Hollow nanoshell formation and collapse in binary solid solutions with large range of solubility

2009 J. Phys.: Condens. Matter 21 415303

(http://iopscience.iop.org/0953-8984/21/41/415303)

J. Phys.: Condens. Matter **21** (2009) 415303 (11pp) doi:10.1088/0953-8984/21/41/415303

Hollow nanoshell formation and collapse in binary solid solutions with large range of solubility

A M Gusak and T V Zaporozhets

Cherkasy National University, 81, Boulevard Shevchenko, Cherkasy, 18031, Ukraine

E-mail: gusak@cdu.edu.ua and tvz@phys.cdu.edu.ua

Received 27 May 2009, in final form 29 July 2009
Published 23 September 2009
Online at stacks.iop.org/JPhysCM/21/415303

Abstract
The formation of a solid solution hollow nanoshell from core–shell structure and collapse of this nanoshell into a compact particle is modelled by a phenomenological scheme and by Monte Carlo simulation. The cross-over between formation and collapse, and the criteria of nanoshell formation are analysed.

(Some figures in this article are in colour only in the electronic version)

M This article features online multimedia enhancements

1. Introduction

Void formation upon reactive diffusion in samples with a closed geometry (cylindrical or spherical) has been known for a long time. It is a common feature of interdiffusion in binary systems and is most frequently related to the difference of partial diffusivities of the components. Such a difference leads to a difference of intrinsic atomic fluxes (in the lattice reference frame) creating the vacancy flux directed toward a faster component. Since the vacancy flux has some spatial distribution (with a maximum in the vicinity of the initial contact zone), it has nonzero divergence, leading to a local accumulation of vacancies on the fast component side and a depletion of vacancies on the slow component side. If vacancy sinks at the fast component side are not effective enough then extra vacancies should gather into voids. Such voiding should be especially pronounced in spherical and cylindrical samples when the faster component is situated inside (figure 1(a)).

This possibility was realized by Aldinger [1], who obtained hollow shells of a BeNi alloy after annealing Be microparticles coated with Ni. Moreover, Geguzin, in his monograph 'Diffusion Zone' (1979) reported the formation of hollow intermetallic wires by the reaction $Cd + Ni \rightarrow Cd_{23}Ni_5$ in a Cd wire covered by Ni [2, 3]. The authors of [2, 3] ascribed this phenomenon to a large step in molar volume in the intermetallic formation (about 8%).

In 2004 void formation in spherical samples was rediscovered at the nanolevel in [4–6]. Hollow nanoshells of cobalt and iron oxides and sulfides have been obtained by means of a reaction of metallic nanopowders with oxygen or sulfur. Contrary to [2, 3], these results have been explained by the Frenkel effect—out-diffusion of metal through the forming spherical layer of the compound is faster than in-diffusion of oxygen or sulfur through the same phase. This inequality of fluxes generates an inward flux of vacancies, meeting inside and forming the void in the central part of the system (figure 1(a)). The Frenkel effect is often called Kirkendall voiding, and this sometimes leads to confusion, since Kirkendall voiding and Kirkendall shift are in fact two different effects, and moreover, two competing effects, competing consequences of the same reason (the difference of partial diffusivities). To emphasize the competing character of Frenkel voiding and Kirkendall shift, Geguzin even introduced special notation for vacancy sinks/sources—K-sinks and F-sinks. K-sinks are, for example, the kinks at dislocations. Vacancies can be annihilated or generated at these K-sinks, locally changing the number of lattice sites and generating a dislocation gradient and a corresponding lattice shift (Kirkendall effect). F-sinks are voids. Vacancies can join these F-sinks without changing the lattice sites number but increasing the total volume. The functioning of F-sinks leads to voiding instead of the Kirkendall shift. If one applies a comparatively low pressure of about 5–10 MPa, which does not considerably change the jump frequency but is sufficient to suppress the void nucleation and/or growth, then one will

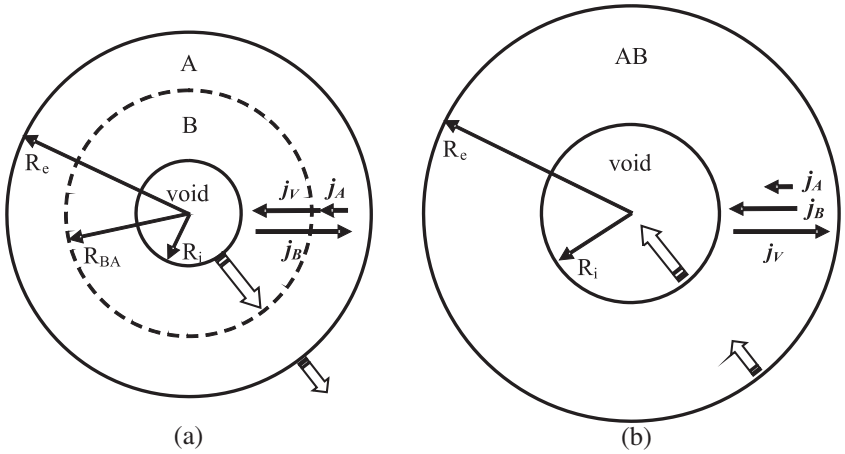

Figure 1. Scheme of formation (a) and collapse (b) of hollow nanoparticle. In the first stage (formation) the vacancy flux is directed inside, opposite to the flux of the faster component B. In the second stage (collapse), when the chemical potential gradient becomes smaller, the Gibbs–Thomson effect prevails: vacancy flux changes direction and flows from the inner surface (with a higher vacancy concentration) to the external surface (with a lower vacancy concentration). The vacancy flux generates opposite fluxes of A and B, with the B-flux being larger, leading to a redistribution—segregation of the faster component B at the inner surface.

suppress the Frenkel effect and observe the 'pure' Kirkendall effect. Indeed, such experiments were made by the Geguzin group and they demonstrated an increase of the Kirkendall shift by a factor of approximately two with almost full suppression of voiding [2].

In hollow nanoshell formation we have the opposite phenomenon—an almost pure Frenkel effect with a fully or partially suppressed Kirkendall shift. Most probably, this happens due to peculiarities of interdiffusion in nanosystems: (1) there is little place for dislocations in a nanoparticle so that K-sinks are just lacking; (2) the common Kirkendall shift in the radial direction leads to tangential deformation and corresponding stresses in spherical or cylindrical samples, which turn out to be large in the case of nanosystems, and suppress the shift.

Just after publication of the first experimental paper on hollow nanoshell formation [4], Tu and Goesele argued that such a hollow structure should be unstable since shrinkage of a hollow shell is energetically favourable (the total surface and surface energy decreases) [7]. The mechanism of shrinkage is related to the Gibbs–Thomson effect (the effect of Laplace pressure on the boundary vacancy concentrations): the vacancy concentration on the inner boundary of the nanoshell should be higher than that on the external boundary. This difference of boundary concentrations leads to an outward vacancy flux meaning shrinking. In [8] we argued that, contrary to shrinking of single-component shell, shrinking of a binary compound shell is also effected by the inverse Kirkendall effect. Namely, an outward vacancy flux generates opposite fluxes of two components, which are different due to their different mobilities (figure 1(b)). In its turn, it leads to segregation of the faster component near the inner boundary. The corresponding concentration gradient substantially suppresses the vacancy flux. Therefore, the shrinkage rate of the compound shell is controlled by the slow species. Shrinkage of compound shells was experimentally verified by Nakamura *et al* [9]. In [10] we analysed the formation of a hollow compound nanoshell. We demonstrated that the Gibbs–Thomson effect, leading to shrinkage of 'ready' compound shells, should be important at the formation stage as well—it sometimes may even suppress the nanoshell formation.

Both previous papers [9] and [10] treated compound shells with a very narrow homogeneity range. For this case the steady-state approximation for both vacancies and main components worked well. Here we will analyse the formation and collapse of a hollow shell in a system with full solubility or, at least, with a broad homogeneity range. In this case one can expect that formation and collapse should be two stages of one whole process—at the first stage (when the chemical driving forces are still large) Kirkendall voiding wins over the curvature effect, then, after arriving at a sufficiently small concentration gradient, the curvature driven shrinking should take its revenge. We will use phenomenological and Monte Carlo modelling, giving the possibility to observe both stages (formation and collapse) in one run. In all mentioned models the peculiarities of diffusion in oxides or sulfides are neglected. These peculiarities will be treated elsewhere.

2. Phenomenological models

In this section we suggest the phenomenological models for both steps of the process—formation of a hollow nanoshell during interdiffusion and shrinking of this newly formed nanoshell with transformation into a compact particle. The description of shrinking looks simpler. Therefore we start with the model of collapse, and then modify this model to describe the formation stage.

2.1. Shrinking

We consider interdiffusion and vacancy fluxes in the spherical hollow nanoparticle, consisting of a binary solid solution with a broad homogeneity range. As was explored in [8], such a shell should shrink due to the outward vacancy flux generated by the

difference of vacancy concentrations at the inner and external boundaries. The vacancy flux should lead to a redistribution of the main components with the corresponding feedback of the created concentration gradient on the vacancy flux and on the corresponding shrinking rate. Contrary to the case of an almost stoichiometric compound [8], in our case of a solid solution we cannot take diffusivities and concentrations as almost constant. Thus, one has to solve the coupled non-linear problem of vacancy flux, interdiffusion and boundary motion. The *following approximations* will be used.

(A1). Tracer diffusivities of both components are proportional to the local vacancy concentration (fraction of empty sites):

$$D^*_{\mathrm{A}}(c) = c_{\mathrm{V}} K_{\mathrm{A}}(c), \qquad D^*_{\mathrm{B}}(c) = c_{\mathrm{V}} K_{\mathrm{B}}(c). \tag{1}$$

Here the concentration c is the molar fraction of component B.

(A2). The composition dependence of both diffusivities is taken as an exponential one, which is typical. For simplicity (just to limit the number of model parameters) the logarithms of both diffusivities are treated as linear functions of the concentration.

$$K_{\mathrm{A}}(c) = K_{\mathrm{A0}} \exp(\alpha_{\mathrm{A}} c_{\mathrm{B}}), \quad K_{\mathrm{B}}(c) = K_{\mathrm{B0}} \exp(\alpha_{\mathrm{B}} c_{\mathrm{B}}). \tag{2}$$

(A3). The diffusion fluxes of the main components and of the vacancies take into account the cross-terms and are written in the lattice reference frame [2, 11]:

$$\Omega j_{\mathrm{A}}(r) = -D^*_{\mathrm{A}} \varphi \frac{\partial c_{\mathrm{A}}}{\partial r} + \frac{c_{\mathrm{A}} D^*_{\mathrm{A}}}{c_{\mathrm{V}}} \frac{\partial c_{\mathrm{V}}}{\partial r} = +K_{\mathrm{A}} \varphi c_{\mathrm{V}} \frac{\partial c_{\mathrm{B}}}{\partial r} + c_{\mathrm{A}} K_{\mathrm{A}} \frac{\partial c_{\mathrm{V}}}{\partial r}, \tag{3A}$$

$$\Omega j_{\mathrm{B}}(r) = -D^*_{\mathrm{B}} \varphi \frac{\partial c_{\mathrm{B}}}{\partial r} + \frac{c_{\mathrm{B}} D^*_{\mathrm{B}}}{c_{\mathrm{V}}} \frac{\partial c_{\mathrm{V}}}{\partial r} = -K_{\mathrm{B}} \varphi c_{\mathrm{V}} \frac{\partial c_{\mathrm{B}}}{\partial r} + c_{\mathrm{B}} K_{\mathrm{B}} \frac{\partial c_{\mathrm{V}}}{\partial r}, \tag{3B}$$

$$\Omega j_{\mathrm{V}}(r) = (K_{\mathrm{B}} - K_{\mathrm{A}}) \varphi c_{\mathrm{V}} \frac{\partial c_{\mathrm{B}}}{\partial r} - (c_{\mathrm{A}} K_{\mathrm{A}} + c_{\mathrm{B}} K_{\mathrm{B}}) \frac{\partial c_{\mathrm{V}}}{\partial r}, \tag{3V}$$

φ is a thermodynamic factor, $\varphi = \frac{c_{\mathrm{A}} c_{\mathrm{B}}}{kT} \frac{\partial^2 g}{\partial c_{\mathrm{B}}^2}$, g is a Gibbs free energy per atom of the solution. In the model of regular solution (Z—coordination number, E_{AA}, E_{BB}, E_{AB}—pair interaction energies between atoms of corresponding kinds):

$$\varphi = 1 + c_{\mathrm{A}} c_{\mathrm{B}} \underbrace{\frac{2Z}{kT} \left(\frac{E_{\mathrm{AA}} + E_{\mathrm{BB}}}{2} - E_{\mathrm{AB}} \right)}_{-\lambda} \equiv 1 + c_{\mathrm{A}} c_{\mathrm{B}} (-\lambda). \tag{4}$$

Here Manning's corrections due to the effect of a vacancy wind are neglected. Our preliminary estimates have shown that these corrections, at least for a disordered solution, do not change the general picture. In this approximation $c_{\mathrm{A}} K_{\mathrm{A}} + c_{\mathrm{B}} K_{\mathrm{B}} = D_{\mathrm{V}}$ (neglecting the correlation factor). The factor λ is proportional to the mixing enthalpy and is negative if solution formation is energetically favourable.

(A4). There is no Kirkendall shift inside the nanoshell. First, as was mentioned in section 1, there is little place for vacancy sinks/sources in a nano-volume. Second, if all atoms of the lattice try to move along the radial direction, this shift would immediately generate tangential deformation and corresponding stresses. Boundaries of the shell do move but not due to lattice shift—just some atoms leave one boundary and attach to another boundary.

Therefore we can write down the continuity equations (analogue of Fick's second law) in the lattice reference frame:

$$\frac{\partial c_{\mathrm{V}}}{\partial t} = -\frac{1}{r^2} \frac{\partial}{\partial r} (r^2 \Omega j_{\mathrm{V}}) + 0, \tag{5V}$$

$$\frac{\partial c_{\mathrm{B}}}{\partial t} = -\frac{1}{r^2} \frac{\partial}{\partial r} (r^2 \Omega j_{\mathrm{B}}). \tag{5B}$$

The zero in equation (5V) was put just there to remind us about the absence or ineffectiveness of vacancy sources and sinks inside the shell.

Boundary conditions. Though $c_{\mathrm{V}}(r, t)$ is a nonequilibrium vacancy distribution, its values at the boundaries are in equilibrium and fixed by the Gibbs–Thomson relation (figure 1(b)):

$$c_{\mathrm{V}}(R_{\mathrm{i}}) = c_{\mathrm{V}}^{\mathrm{eq}} \exp\left(+\frac{2\gamma\Omega}{kT} \frac{1}{R_{\mathrm{i}}} \right), \qquad c_{\mathrm{V}}(R_{\mathrm{e}}) = c_{\mathrm{V}}^{\mathrm{eq}} \exp\left(-\frac{2\gamma\Omega}{kT} \frac{1}{R_{\mathrm{e}}} \right). \tag{6}$$

The flux balance equations at the moving inner and external boundaries depend on the conditions of the experiment. Here we will treat the case when evaporation of atoms from the nanoshell is impossible. So, all fluxes outside the shell and inside the central void are absent. A vacancy flux from the inner boundary to the external boundary generates the movement of both these boundaries according to trivial relations:

$$\frac{\mathrm{d}R_{\mathrm{i}}}{\mathrm{d}t} = -\Omega j_{\mathrm{V}}(R_{\mathrm{i}}), \qquad \frac{\mathrm{d}R_{\mathrm{e}}}{\mathrm{d}t} = -\Omega j_{\mathrm{V}}(R_{\mathrm{e}}). \tag{7}$$

Boundary conditions (6) and (7) would be enough for shrinking of a single-component shell. In our case of a binary solution we should have additional conditions. Boundary concentrations of the main components are not fixed (we do not have an analogue of equation (6) for A or B), but the conservation laws are valid, of course, implying the conditions on fluxes. The sum of three fluxes is zero in the lattice reference frame ($j_{\mathrm{V}} + j_{\mathrm{A}} + j_{\mathrm{B}} = 0$). Thus, two fluxes are independent. It means that one should write down the flux balance equations at both moving boundaries for one of the main components, taking into account that fluxes outside the shell equal zero:

$$(c_{\mathrm{B}}(R_{\mathrm{i}}) - 0) \frac{\mathrm{d}R_{\mathrm{i}}}{\mathrm{d}t} = \Omega j_{\mathrm{B}}(R_{\mathrm{i}}) - 0, \qquad (c_{\mathrm{B}}(R_{\mathrm{e}}) - 0) \frac{\mathrm{d}R_{\mathrm{e}}}{\mathrm{d}t} = \Omega j_{\mathrm{B}}(R_{\mathrm{e}}) - 0. \tag{8}$$

Combining equations (7) and (8), one gets:

$$-c_{\mathrm{B}}(R_{\mathrm{i}}) \Omega j_{\mathrm{V}} = \Omega j_{\mathrm{B}}(R_{\mathrm{i}}), \qquad -c_{\mathrm{B}}(R_{\mathrm{e}}) \Omega j_{\mathrm{V}} = \Omega j_{\mathrm{B}}(R_{\mathrm{e}}). \tag{9}$$

Below we will use common steady-state approximation for fast diffusing vacancies, which reflects the hierarchy of characteristic times—the vacancy subsystem is fast enough to adapt to the slow redistribution of the main components and to movement of the boundaries (except at the very last stage of collapse, which is very fast):

$$\frac{\partial C_V}{\partial t} \approx 0 \Rightarrow r^2 \Omega j_V(r) = \frac{\Omega J_V}{4\pi} = \text{const at } r. \tag{10}$$

(J_V is the total flux of vacancies which has to be determined from boundary conditions).

It is convenient now to make the following transformation of variables:

$$t' = t; \qquad \xi = \frac{1/r - 1/R_e}{1/R_i - 1/R_e}, \qquad 0 < \xi < 1, \tag{11}$$

$$\frac{\partial}{\partial t} = \frac{\partial}{\partial t'} + \left(\frac{\xi}{R_i^2}\frac{dR_i}{dt} + \frac{(1-\xi)}{R_e^2}\frac{dR_e}{dt} \right) \frac{R_e R_i}{R_e - R_i}\frac{\partial}{\partial \xi},$$
$$\frac{\partial}{\partial r} = -\frac{[R_i + (R_e - R_i)\xi]^2}{(R_e - R_i)R_e R_i}\frac{\partial}{\partial \xi}. \tag{12}$$

Using equations (3V), (11), (12) one obtains:

$$\Omega J_V/4\pi = \frac{R_e R_i}{R_e - R_i}\left(-(K_B - K_A)\varphi c_V \frac{\partial c_B}{\partial \xi} + (c_A K_A + c_B K_B)\frac{\partial c_V}{\partial \xi} \right), \qquad \text{or} \tag{13}$$

$$\frac{\partial c_V}{\partial \xi} = \frac{(K_B - K_A)\varphi}{c_A K_A + c_B K_B} c_V \frac{\partial c_B}{\partial \xi} + \frac{(\Omega J_V/4\pi)}{c_A K_A + c_B K_B}\frac{(R_e - R_i)}{R_e R_i}.$$

If $c_B(\xi)$ profile is known, then equation (13) has a standard form:

$$\frac{dc_V(\xi)}{d\xi} = f(\xi)c_V + \frac{a}{\psi(\xi)} \tag{14}$$

with

$$\psi(\xi) = c_A(\xi)K_A(\xi) + c_B(\xi)K_B(\xi),$$
$$f(\xi) = \frac{(K_B - K_A)\,\varphi}{c_A K_A + c_B K_B}\frac{\partial c_B}{\partial \xi}, \tag{15}$$

and can be solved with respect to the unknown function $c_V(\xi)$:

$$c_V(\xi) = \exp\left(\int_0^\xi f(\xi')\,d\xi' \right)\left(c_v^{eq} \exp\left(-\frac{2\gamma\Omega}{kTR_e} \right) + \frac{R_e - R_i}{R_e R_i}\frac{\Omega J_V}{4\pi}\int_0^\xi \frac{d\xi'}{\psi(\xi')} \exp\left(-\int_0^{\xi'} f(\xi'')\,d\xi'' \right) \right). \tag{16}$$

Combining expression (16) with the Gibbs–Thomson relations (6) for boundary vacancy concentrations, we obtain an expression for the total vacancy flux in terms of the unknown B-concentration profile:

$$\frac{\Omega J_V}{4\pi} = \frac{R_e R_i}{R_e - R_i} c_v^{eq} \times \frac{\exp\left(\frac{2\gamma\Omega}{kTR_i}\right)\exp(-\int_0^1 f(\xi)\,d\xi) - \exp\left(-\frac{2\gamma\Omega}{kTR_e}\right)}{\int_0^1 \exp\left(-\int_0^\xi f(\xi')\,d\xi'\right)\frac{d\xi}{\psi(\xi)}}. \tag{17}$$

Substituting equation (13) into equation (3B), one can express the flux of one of the main components in terms of its gradient and of total vacancy flux (which is constant within the layer):

$$r^2\Omega j_B(r) = -K_B\varphi c_V r^2\frac{\partial c_B}{\partial r} + c_B K_B r^2 \frac{\partial c_V}{\partial r} = \frac{R_e R_i}{(R_e - R_i)}\left(K_B\varphi c_V \frac{\partial c_B}{\partial \xi} - c_B K_B \frac{\partial c_V}{\partial \xi} \right) = \frac{R_e R_i}{(R_e - R_i)}\frac{K_A K_B \varphi}{c_A K_A + c_B K_B} c_V \frac{\partial c_B}{\partial \xi} - \frac{c_B K_B}{c_A K_A + c_B K_B}\frac{\Omega J_V}{4\pi}. \tag{18}$$

Thus, the steady-state approximation for vacancies, together with the Gibbs–Thomson boundary conditions, reduces the system of two differential equations (4) and (5V), (5B) to only one, however, integro-differential equation:

$$\frac{\partial c_B}{\partial t'} = \frac{\xi\frac{d\eta_i}{dt} + (1-\xi)\frac{d\eta_e}{dt}}{\eta_i - \eta_e}\frac{\partial c_B}{\partial \xi} + \frac{(\eta_e + (\eta_i - \eta_e)\xi)^4}{(\eta_i - \eta_e)^2}\frac{\partial}{\partial \xi}\left(\frac{K_A K_B \varphi(\xi)}{c_A K_A + c_B K_B} c_V(\xi)\frac{\partial c_B}{\partial \xi} - \frac{c_B K_B}{c_A K_A + c_B K_B}(\eta_i - \eta_e)\frac{\Omega J_V}{4\pi} \right) \tag{19}$$

with $\eta_i = 1/R_i$, $\eta_e = 1/R_e$.

The total vacancy flux in equation (19) is determined by equation (17). The conditions for the B-profile at the internal ($\xi = 1$) and external ($\xi = 0$) boundaries can be found from equation (9) with using equations (17) and (18):

$$\left.\frac{\partial c_B}{\partial \xi}\right|_{\xi=1} = -\frac{R_e - R_i}{R_e R_i}\frac{\Omega J_V}{4\pi}\left[\frac{c_A c_B (K_B - K_A)}{K_A K_B \varphi} \right]_{\xi=1} \times \exp\left(-\frac{2\gamma\Omega}{kTR_i} \right) \Big/ c_V^{eq}, \tag{20}$$

$$\left.\frac{\partial c_B}{\partial \xi}\right|_{\xi=0} = -\frac{R_e - R_i}{R_e R_i}\frac{\Omega J_V}{4\pi}\left[\frac{c_A c_B (K_B - K_A)}{K_A K_B \varphi} \right]_{\xi=0} \times \exp\left(+\frac{2\gamma\Omega}{kTR_e} \right) \Big/ c_V^{eq}. \tag{21}$$

The boundary problem (19)–(21) is solved by the explicit finite-difference scheme, with the B-profile at a previous time step used for the calculation of the total vacancy flux according to equation (17) and substituted into equation (19) for calculating the profile at the next time step. After this the newly calculated B-profile is used to calculate the new vacancy profile according to equation (16). The velocities of the boundaries, and the new internal and external radii are calculated according to equation (7), also from the newly found value of the total vacancy flux.

2.2. Formation of a hollow nanoshell from the core–shell structure without the influence of the atmosphere (ambient)

To describe the formation of a nanoshell, we do not need to change the model equations—we only change the initial conditions. Namely, consider a sphere of pure B of radius R_{BA} surrounded by a shell of pure A (figure 1(a)). To escape solving the nucleation problem, let us assume that the initial pure sphere A already contains a small void in the centre. Of course, for too big an initial core this assumption seems unreasonable

since the first voids should nucleate in the vicinity of the initial contact between A and B. Yet, for nanoparticles it is natural that the initial nanovoids coalesce very fast into a single central void. Thus, in our model the initial B-profile is:

$$t' = 0, \qquad c_{\mathrm{B}}(\xi) = \begin{cases} 1, & 0 < \xi < \xi_{\mathrm{BA}} \\ 0, & \xi_{\mathrm{BA}} < \xi < 1, \end{cases} \qquad \xi_{\mathrm{BA}} \equiv \frac{1/R_{\mathrm{BA}} - 1/R_{\mathrm{e0}}}{1/R_{\mathrm{i0}} - 1/R_{\mathrm{e0}}}. \tag{22}$$

Evidently, the curvature effect, determining the kinetics of collapse at the shrinking stage, cannot be neglected at the formation stage as well. Formation of a nanoshell is a result of competition between the Frenkel effect due to chemical forces (and the difference of diffusivities) and the Gibbs–Thomson effect, as discussed in [10]. The smaller the radius, the larger should be the role of curvature driven effects. Thus, one can expect that, for an initial void radius smaller than some critical value, formation will be impossible. This critical radius can be found from the expression (17) for vacancy flux. Namely, an initial pore in the B/A core shell structure will shrink from the very beginning if the sign of the vacancy flux is positive. For this it is necessary that

$$\exp\left(\frac{2\gamma\Omega}{kTR_{\mathrm{i}}}\right)\exp\left(-\int_0^1 f(\xi)\,\mathrm{d}\xi\right) > \exp\left(-\frac{2\gamma\Omega}{kTR_{\mathrm{e}}}\right), \tag{23}$$

which means:

$$\int_{c_{\mathrm{B}}(R_{\mathrm{e}})}^{c_{\mathrm{B}}(R_{\mathrm{i}})} \frac{(K_{\mathrm{B}} - K_{\mathrm{A}})\,(1 - \tilde{n}_{\mathrm{A}} c_{\mathrm{B}}\lambda)}{c_{\mathrm{A}}K_{\mathrm{A}} + c_{\mathrm{B}}K_{\mathrm{B}}}\,\mathrm{d}c_{\mathrm{B}} < L\left(\frac{1}{R_{\mathrm{i}}} + \frac{1}{R_{\mathrm{e}}}\right), \qquad L = \frac{2\gamma\Omega}{kT}. \tag{24}$$

At the very beginning $c_{\mathrm{B}}(R_{\mathrm{e}}) = 0$, $c_{\mathrm{B}}(R_{\mathrm{i}}) = 1$. Thus, formation of a hollow nanoshell from a core–shell structure is forbidden if

$$\frac{1}{R_{\mathrm{i}}} + \frac{1}{R_{\mathrm{e}}} > \frac{1}{L}\int_0^1 \frac{(\kappa \mathrm{e}^{\alpha x} - 1)(1 - \lambda x(1-x))}{1 + x(\kappa \mathrm{e}^{\alpha x} - 1)}\,\mathrm{d}x. \tag{25}$$

Here $\kappa = \frac{K_{\mathrm{B0}}}{K_{\mathrm{A0}}}$, $\alpha = \alpha_{\mathrm{B}} - \alpha_{\mathrm{A}}$, $x = c_{\mathrm{B}}$.

This criterion is not rigorous since it was obtained under two major assumptions: (a) a steady-state approximation for vacancies and (b) the assumption of a single central void preexisting in the centre and serving as the sink for all extra vacancies coming into the B-rich core. In reality, at the very beginning the largest supersaturation with vacancies should appear just under the initial contact surface B/A, as will be seen in figure 5 (vacancy profile at the initial formation stage). It may lead to several tiny voids forming under the B/A perimeter, as we will see later in the Monte Carlo simulation and as was observed in experiments at low temperatures [6].

3. Results of phenomenological model

In figure 2 one can see that the time law of shrinking correlates with the time dependence of the segregation

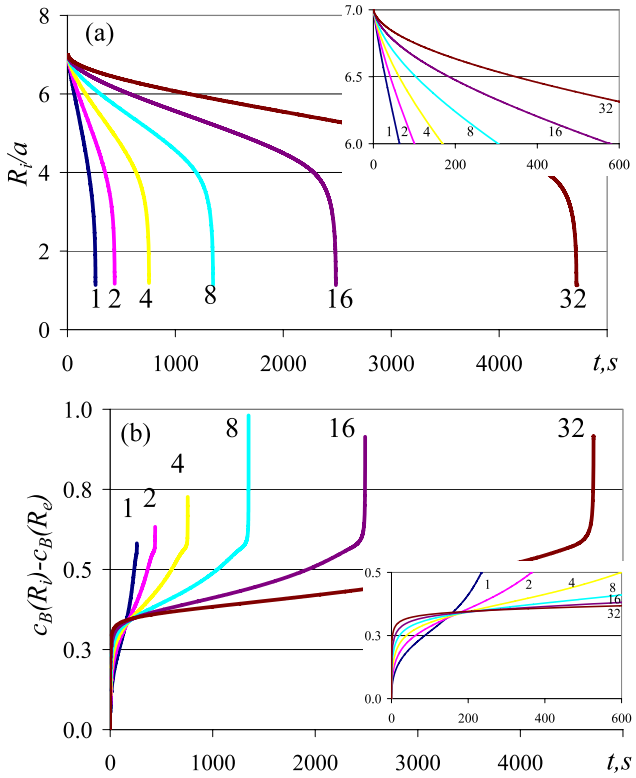

Figure 2. Time dependences of void radius (a) and segregation magnitude (b) during shrinking at various ratios of diffusivities $\kappa = 1, 2, 4, 8, 16, 32$ (actually, preexponential factors)—phenomenological model. Parameters: $c_{\mathrm{V}}^{\mathrm{eq}} = 10^{-4}$, $c_{\mathrm{B}}^{\mathrm{init}} = 0.5$, $R_{\mathrm{i}}^{\mathrm{init}} = a$, $R_{\mathrm{e}}^{\mathrm{init}} = 17a$, $L = 10^{-9}$ m, $\kappa = 10$, $\alpha_{\mathrm{A}} = -6$, $\alpha_{\mathrm{B}} = -2$, $\lambda = 0$.

magnitude measured as the difference between the B-species concentration at the external and internal nanoshell boundaries (a—lattice parameter, used in Monte Carlo simulation, section 4). Also, one can notice a peculiarity in the time dependence just after the initial stage. The shrinking rate slows down after a rather fast initial segregation—the $R_{\mathrm{i}}(t)$ dependence has an inflection point. Later we will see that this peculiarity is not general, and disappears in the cross-over regime when the nanoshell collapse follows the nanoshell formation at the same temperature. We believe that the reason is related to different initial conditions. The results shown in figure 2 are obtained for a rather artificial initial condition, when the initial concentration is taken equal everywhere. So, some short period of adjustment follows. If we take a just grown nanoshell, it has an inhomogeneous concentration distribution from the very beginning (because of the competition of Kirkendall, inverse Kirkendall and Gibbs–Thomson effects proceeds at the formation stage as well). So, one can expect a constant sign of the second time derivative in this case (see figure 5).

The time of full collapse depends almost linearly on the ratio κ of preexponential factors in equation (2): $t_{\mathrm{collapse}} = m\kappa + b$. The magnitudes of coefficients m and b in this linear approximation change at small mixing enthalpies and reach asymptotic values at large mixing enthalpies (figure 3).

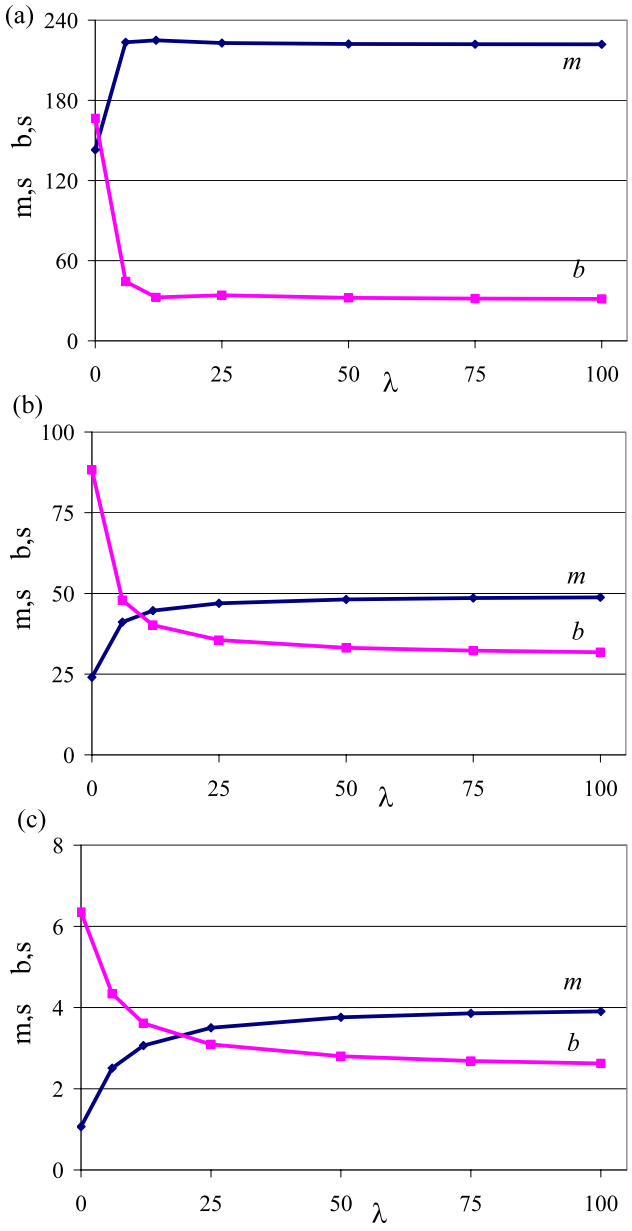

Figure 3. Dependences of the parameters m and b of the linear approximation $t_{\text{collapse}} = m\kappa + b$ ($\kappa = 1, 2, 4, 8, 16, 32$) for the collapse time t_{collapse} on non-dimensional mixing enthalpy—phenomenological model. Parameters: $c_{\text{v}}^{\text{eq}} = 10^{-4}$, $c_{\text{B}}^{\text{init}} = 0.5$, $R_{\text{i}}^{\text{init}} = a$, $R_{\text{e}}^{\text{init}} = 17a$, $L = 10^{-9}$ m, $\lambda = 0, 6, 12, 25, 50, 100$ and (a) $\alpha_{\text{A}} = -6$, $\alpha_{\text{B}} = -2$; (b) $\alpha_{\text{A}} = -3$, $\alpha_{\text{B}} = -2$; (c) $\alpha_{\text{A}} = 2$, $\alpha_{\text{B}} = 3$.

Such a linear dependence was predicted by us in the case of compound nanoshells with a very narrow homogeneity range [8]:

$$t_{\text{collapse}} \approx \frac{kT}{12\gamma\Omega} r_{\text{f}}^3 \frac{C_{\text{A}} D_{\text{B}}^* + C_{\text{B}} D_{\text{A}}^*}{D_{\text{A}}^* D_{\text{B}}^*} = \frac{kT}{12\gamma\Omega} \frac{r_{\text{f}}^3}{D_{\text{B}}^*} \times \left((1 - C_{\text{B}}) \frac{D_{\text{B}}^*}{D_{\text{A}}^*} + C_{\text{B}} \right) \tag{26}$$

(r_{f} is a final particle radius after collapse).

In our case $\frac{D_{\text{B}}^*}{D_{\text{A}}^*} = \kappa \exp((\alpha_{\text{B}} - \alpha_{\text{A}})c_{\text{B}})$. Thus, in the case of a narrow compound phase (meaning a large mixing enthalpy) one can expect that

$$\frac{m}{b} = \frac{1 - c_{\text{B}}}{c_{\text{B}}} \exp\left((\alpha_{\text{B}} - \alpha_{\text{A}})c_{\text{B}}\right). \tag{27}$$

One can see that the asymptotic values of this ratio in the present case of a solid solution are indeed close to the mentioned analytical prediction (table 1).

Table 1. Asymptotic (at large λ) ratio of linear fit coefficients for the dependence of collapse time on the diffusivity ratio.

α_{A}	α_{B}	m/b, analytical prediction (equation (27))	m/b, phenomenological model
−6	−2	7.07	7.39
−3	−2	1.54	1.65
2	3	1.49	1.65

In figure 4 one can see that the validity of the steady-state approximation for the main components improves with increasing absolute value of mixing enthalpy. To demonstrate this, we compare the value of reduced shrinking rate

$$\text{RSR} = \frac{\mathrm{d}R_{\text{i}}}{\mathrm{d}t} R_{\text{i}}^2 \frac{1/R_{\text{i}} - 1/R_{\text{e}}}{\exp\left(\frac{2\gamma\Omega}{kTR_{\text{i}}}\right) - \exp\left(-\frac{2\gamma\Omega}{kTR_{\text{e}}}\right)}, \tag{28}$$

obtained in our present model, and the value obtained in the steady-state approximation for compounds in [8]:

$$\text{RSR}_0 = \frac{D_{\text{A}}^* D_{\text{B}}^*}{(c_{\text{A}} D_{\text{B}}^* + c_{\text{B}} D_{\text{A}}^*)}, \tag{29}$$

(with tracer diffusivities calculated for initial nanoshell composition before shrinking).

One can see that the larger the absolute value of mixing enthalpy (the larger are the chemical forces) the better the steady-state approximation works. This is an answer to the problem stated by the group of Murch [12].

In figure 5 we demonstrate (for the first time, as far as we know) formation and shrinkage in one run. During the formation stage the chemical forces in a sharply inhomogeneous system are stronger than the curvature driven vacancy gradient. After formation of a partially homogeneous hollow nanoshell, chemical forces become weaker, and the curvature driven Gibbs–Thomson effect wins, leading to a collapse due to the outward vacancy flux.

Profiles of B species in figure 5 demonstrate that the full homogenization is not reached during nanoshell formation—even at maximal void radius the concentration gradient is not zero, and later it grows back due to the inverse Kirkendall effect. The vacancy profile shows the formation of supersaturation just under the initial B/A interface at the initial stage. Later this nonmonotonic profile transforms into a monotonic one.

4. Monte Carlo simulation of the vacancy subsystem evolution in the structure 'core–shell'

Alternatively to the offered phenomenological models, we developed a 3D Monte Carlo model of nanoshell formation and

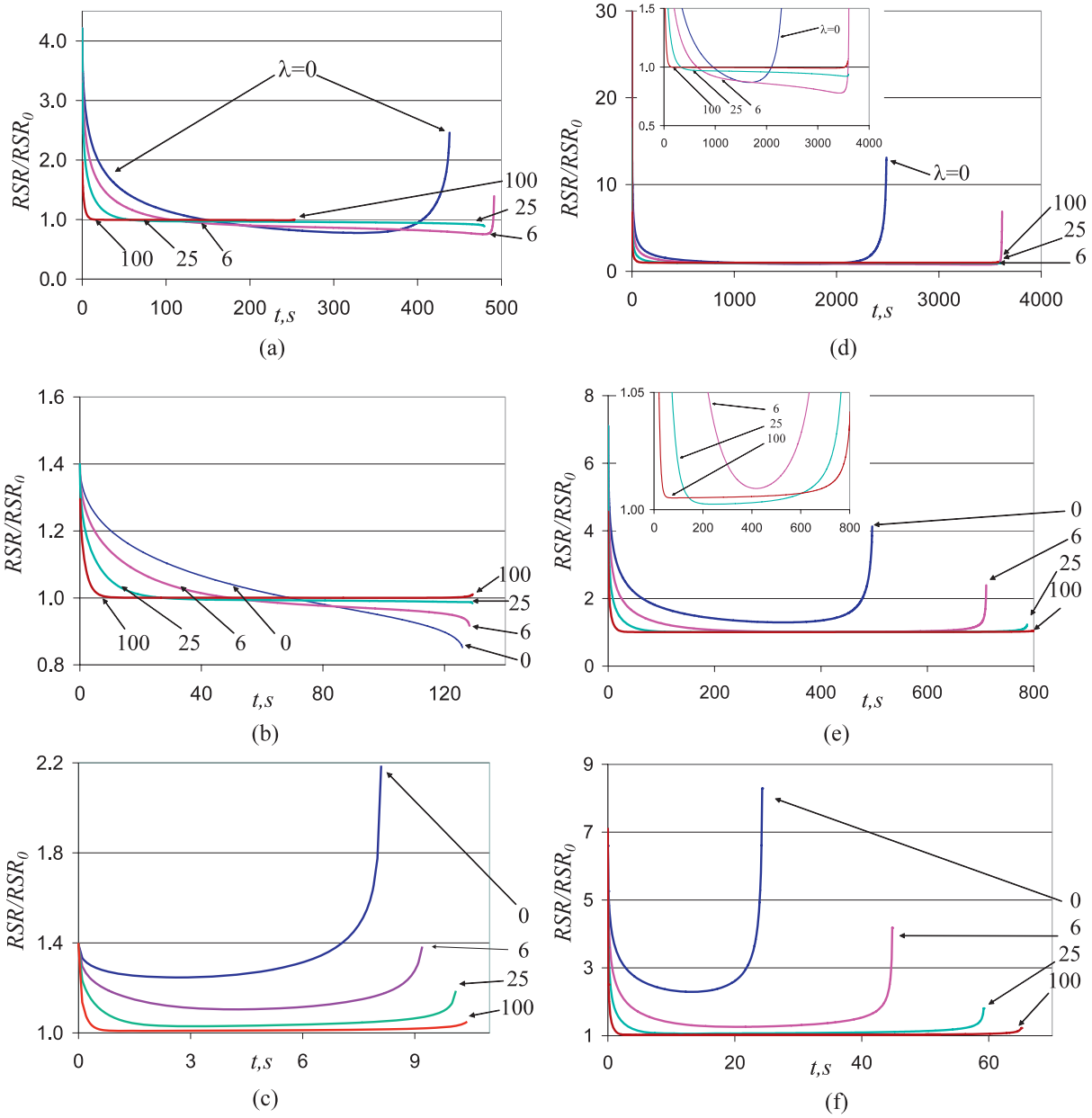

Figure 4. Time dependence of reduced shrinking rate defined by equation (28) at various values of mixing enthalpy $\lambda = 0, 6, 25, 100$ calculated at $c_v^{eq} = 10^{-4}$, $c_B^{init} = 0.5$, $R_i^{init} = a$, $R_e^{init} = 17a$, $L = 10^{-9}$ m and (a) $\kappa = 2$, $\alpha_A = -6$, $\alpha_B = -2$; (b) $\kappa = 2$, $\alpha_A = -3$, $\alpha_B = -2$; (c) $\kappa = 2$, $\alpha_A = 2$, $\alpha_B = 3$; (d) $\kappa = 16$, $\alpha_A = -6$, $\alpha_B = -2$; (e) $\kappa = 16$, $\alpha_A = -3$, $\alpha_B = -2$; (f) $\kappa = 16$, $\alpha_A = 2$, $\alpha_B = 3$.

collapse for the fcc-structure (lattice parameter a) of binary alloy with vacancies. To be sure that the proposed model is valid and the chosen parameters are reasonable, we should check at first, if a hollow nanoshell is indeed formed from the initial core–shell structure.

The difference of diffusivities of A and B species (even in the case of an ideal alloy with zero mixing enthalpy) is provided by the probability of choosing the atom of a given kind in the Metropolis algorithm, determined by the ratio of frequencies $K = \nu_B/\nu_A$ ($\nu_A \leqslant \nu_B$). Actually, the difference of mobilities is stipulated not only by different frequencies K, but also by thermodynamics and the structures of the sublattices: in the ordered phase A_1B_3 the component B will have a higher mobility even in the case of equal frequencies.

Temperature is, typically for MC simulations, regulated by varying the non-dimensional ratio ε of average interaction energy E and kT (larger ε means lower temperature):

$$\varepsilon = c_A^2\varepsilon_{AA} + c_B^2\varepsilon_{BB} + 2c_Ac_B\varepsilon_{AB}. \tag{30}$$

In the following we model the nonideal (with tendency to ordering) as well as ideal solutions, combining the sets of non-dimensional pair interaction energies or/and concentrations to satisfy equation (30) at fixed ε (fixed temperature).

In section 4.1 we simulate the formation of a nanoshell for the case of a nonideal solution. In section 4.2 we simulate the cross-over from formation to collapse, as well for a nonideal solution but for another average concentration, to obtain the formation and collapse in one run in a reasonable computation

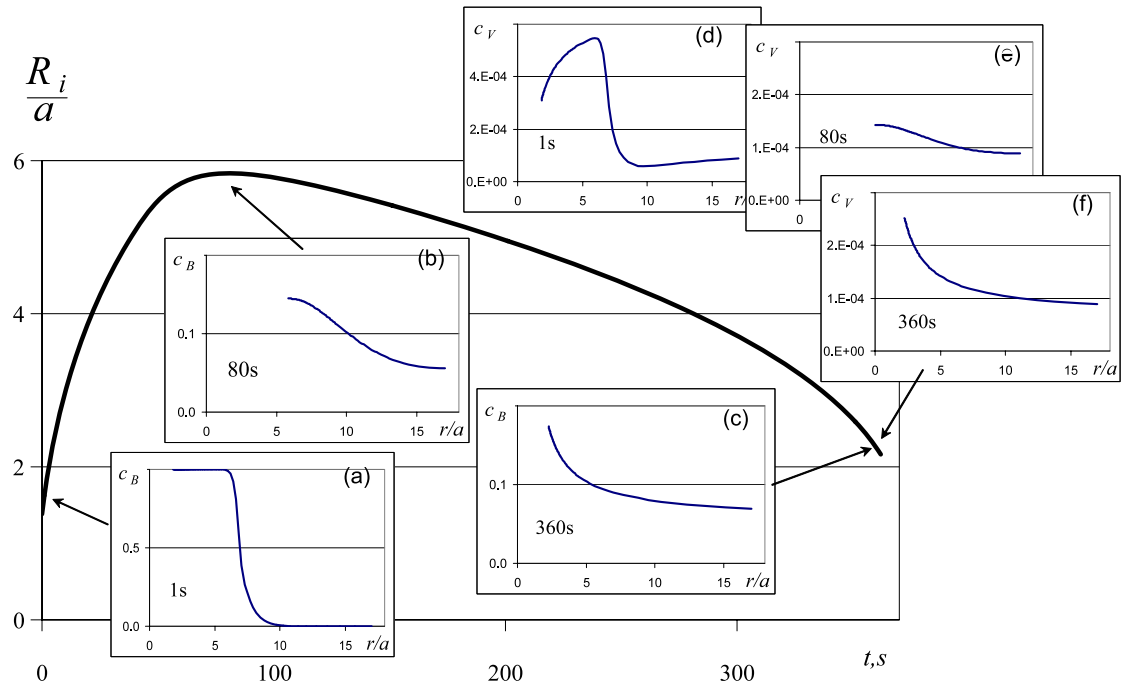

Figure 5. Time evolution of initial tiny void radius—first a fast formation of the hollow nanoshell and then its collapse (slow and then faster and faster). Insets (a)–(c) show the concentration profiles of the faster component at formation, the cross-over and the collapse stages respectively. Insets (d)–(f) show the vacancy concentration profiles at the same stages. One can see that the transition from formation to collapse does not mean the full homogenization of the shell. Parameters: $c_{\mathrm{v}}^{\mathrm{eq}} = 10^{-4}$, $c_{\mathrm{B}}^{\mathrm{init}} = 0.075$, $R_{\mathrm{i}}^{\mathrm{init}} = 1.4a$, $R_{\mathrm{BA}}^{\mathrm{init}} = 7a$, $R_{\mathrm{e}}^{\mathrm{init}} = 17a$, $L = 0.75 \times 10^{-9}$ m, $\kappa = 10$, $\lambda = 0$, $\alpha_{\mathrm{A}} = -4.5$, $\alpha_{\mathrm{B}} = -2$, $\mathrm{d}t = 10^{-4}$ s.

time. In section 4.3 we mainly investigate the segregation caused by the (kinetic reasons) inverse Kirkendall effect—for this reason in this subsection we treat an ideal solution.

4.1. Formation of a nanoshell in the MC-simulation

To investigate the kinetics of nanoshell formation a nanoparticle of pure B component (radius $R_{\mathrm{BA}} = 15.7a$) was initially enveloped by a pure A component (external radius $R_{\mathrm{e}} = 17a$) (total number of atoms is 82 421)—the chosen ratio of internal R_{BA} and external R_{e} concentric radii provides the necessary volume fractions in the eventual A_1B_3 phase ($c_{\mathrm{B}} = 0.75$). According to equation (30) the pair energies in this case are chosen as $\varepsilon_{\mathrm{AA}} = \varepsilon_{\mathrm{BB}} = 0.7\varepsilon_{\mathrm{AB}}$: at low temperature $\varepsilon_{\mathrm{AA}}^{\mathrm{L}} = \varepsilon_{\mathrm{BB}}^{\mathrm{L}} = -1.32$, $\varepsilon_{\mathrm{AB}}^{\mathrm{L}} = -1.89$ with average energy $\varepsilon^{\mathrm{L}} = -1.535$ [13]; at high temperature $\varepsilon_{\mathrm{AA}}^{\mathrm{H}} = \varepsilon_{\mathrm{BB}}^{\mathrm{H}} = -0.86$, $\varepsilon_{\mathrm{AB}}^{\mathrm{H}} = -1.23$ with average energy $\varepsilon^{\mathrm{H}} = -0.98$. As a result of the simulation the widening of the A/B diffusion zone is observed and small voids start forming at the pure B/alloy interface. In the process of the computer experiment the voids expand, leaving between themselves 'bridges' of pure B. At high temperature we observed the subsequent coalescence of voids into a single spherical void in the centre of the nanoparticle (figure 6, movie 1, 'Void Formation', left—cross-section view of nanoparticle, right—transmission view of empty sites, histogram in right up corner is a radial distribution of empty sites, available at stacks.iop.org/JPhysCM/21/415303). These simulation results correlate with the experiments on the formation of cobalt selenides and sulfides [4, 6, 14].

4.2. Cross-over from formation to collapse

In the above mentioned simulations the process practically stopped after formation of the hollow nanoshell. It seems quite clear since formation is driven by chemical forces and collapse—by capillary ones. The latter are usually significantly less than chemical forces. Therefore, shrinking of a nanovoid is typically a much slower process and can be observed at temperatures higher than for the process of formation. To describe the formation and collapse in one simulation, one needs higher temperatures. We took $\varepsilon_{\mathrm{AA}}^{\mathrm{H}}$, $\varepsilon_{\mathrm{BB}}^{\mathrm{H}}$, $\varepsilon_{\mathrm{AB}}^{\mathrm{H}}$ and the initial interrelation of the components' radii $R_{\mathrm{BA}} = 7a$, $R_{\mathrm{e}} = 17a$, corresponding to an average concentration $\bar{c}_{\mathrm{B}} = 0.075$ (5745 B atoms, 76 676 A atoms) and to $\varepsilon = 0.9$. The process of void formation proceeded very quickly (during 1238 MCS). At that point, the void formed in the centre of the nanoparticle and appeared to be unstable: just after having reached the maximal size (3314 sites) it collapsed (figure 7, movie 2, 'Crossover from formation to collapse', available at stacks.iop.org/JPhysCM/21/415303). To correlate the simulation results with the phenomenological model, we recalculated the number of empty sites into an effective void radius R_{i}.

4.3. Shrinking and segregation kinetics in the MC-simulation

Now we come back to synergy of curvature driven effects and the inverse Kirkendall effect at the shrinking stage. The above described MC-model was used to simulate the collapse of the nanoshell with $R_{\mathrm{i}} = 7a$, $R_{\mathrm{e}} = 17a$ (total number of atoms is

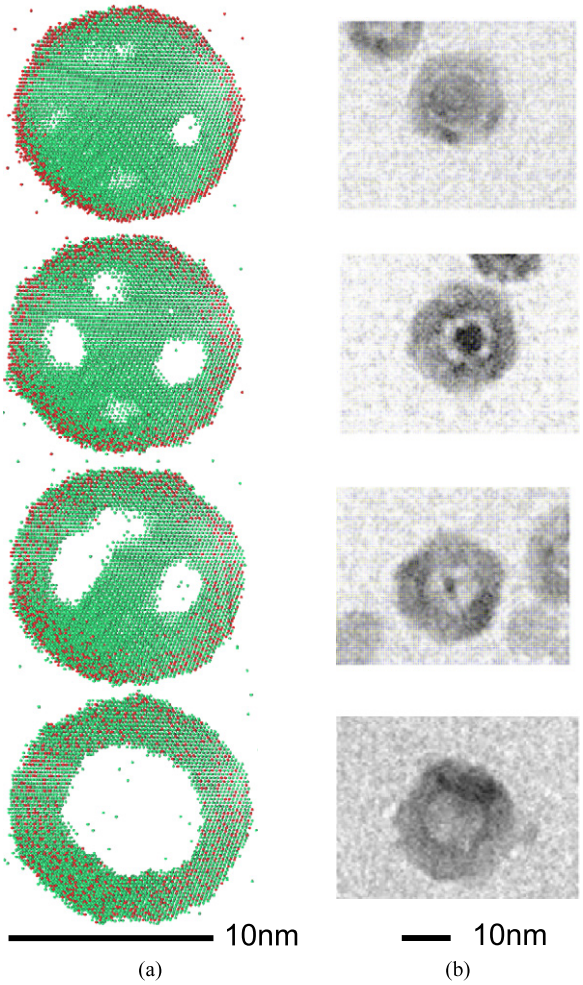

Figure 6. Void formation in a nanoparticle: (a) results of the MC-simulation with $\bar{c}_B = 0.75$, $K = 10$ at high temperature (ε^H) at time points of 167, 1000, 2000 and 10 000 MCS (sample cross-section, light dots—B, dark dots—A), the maximal size of the void attained at 8400 MCS; (b) evolution of CoSe hollow nanocrystals with time by injection of a suspension of selenium in odichlorobenzene into a cobalt nanocrystal solution at 455 K: 10 s, 1, 2 and 30 min [4].

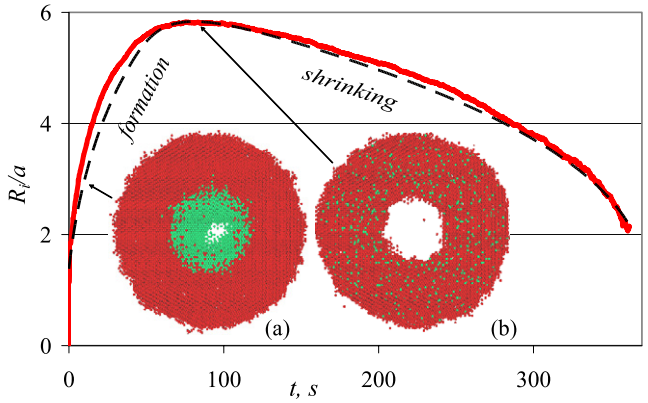

Figure 7. Nanoshell formation and collapse in one run—atomistic simulation and phenomenology. MC (solid line) and phenomenological (dashed line) plots are superimposed with respective time rescaling: 1 MCS = 62 ms. MC-modelling at high temperature (ε^H_{AA}, ε^H_{BB}, ε^H_{AB}), $K = 10$ and a small fraction of a more mobile B component (light dots, $\bar{c}_B = 0.075$): (a) formation stage; (b) cross-over. Phenomenological plot calculated at $c_V^{eq} = 10^{-4}$, $c_B^{init} = 0.075$, $R_i^{init} = 1.4a$, $R_{BA}^{init} = 7a$, $R_e^{init} = 17a$, $L = 0.75 \times 10^{-9}$ m, $\kappa = 10$, $\lambda = 0$, $\alpha_A = -4.5$, $\alpha_B = -2$, $dt = 10^{-4}$ s.

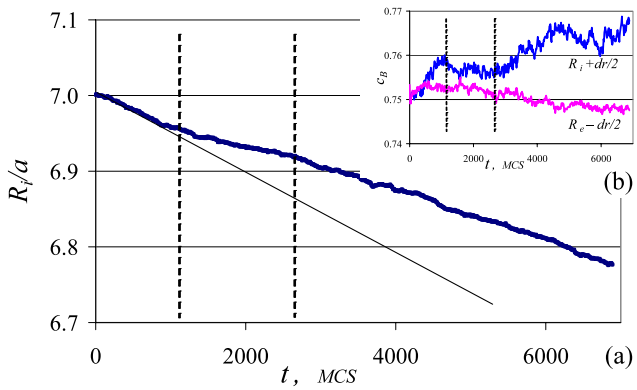

Figure 8. MC-time-dependence of inner radius (a) and of the concentration near the moving boundaries (b) at the initial stage of the shrinkage of the A_1B_3 nanoshell ($R_i = 7a$, $R_e = 17a$, $dr \approx 1.7a$, $K = 10$, ε^H): segregation of B species near the internal surface leads to slowing down of the nanoshell shrinkage.

76 676 and the number of empty sites in the void is 5745) for an ideal alloy at $\bar{c}_B = 0.75$ and $K = 10$. At high temperature (ε^H) after 7000 MCS the void has shrunk by 9.58% (figure 8).

To investigate the segregation effects we have used nanoshells of an ideal alloy with $R_i = 4a$, $R_e = 8a$ at low temperature (ε^L) with different ratios of frequencies K (10, 50, 100) and concentrations c_B (0.25, 0.50, 0.75, 1.00). We may conclude that the larger is K and/or c_B, the more intensive are the segregations of the more mobile component near the internal surface (figure 9) and the slower is the process of nanoshell collapse (figure 10).

5. Conclusion

Formation of hollow nanoshells and their collapse are presented as the two stages of one process with the cross-over between regimes being determined by competition of the Kirkendall driven Frenkel effect, the curvature driven Gibbs–Thomson effect and of the inverse Kirkendall effect. Such a unified approach appears to be reasonable both in the phenomenologic analysis and in Monte Carlo simulation. The presented analysis is applied (in this paper) only to the case of solid solutions. One can formulate the following main features and predictions of the mentioned approach.

(1) Formation of the hollow shell is driven by the inward vacancy flux which contains two competing inputs: (a—assisting formation) chemical driving force which is proportional to the main component's gradient and the difference of partial diffusivities (if the faster component is situated inside), (b—suppressing formation) vacancy gradient created by the difference of equilibrium vacancy concentrations at the inner and external boundaries

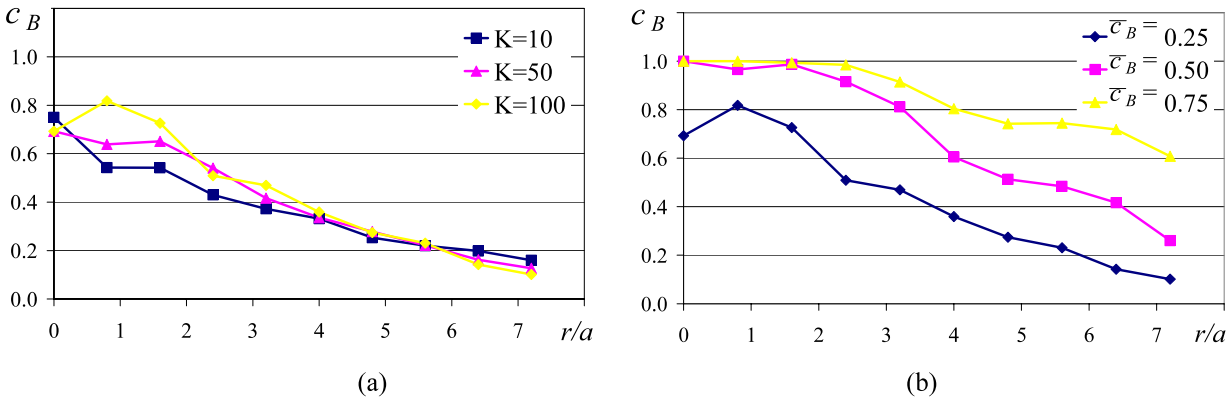

Figure 9. Radial concentration profile for a nanoparticle just after collapse: (a) at different ratios of the frequencies of components (average concentration $\bar{c}_B = 0.25$); (b) at different average concentrations (at $K = 100$).

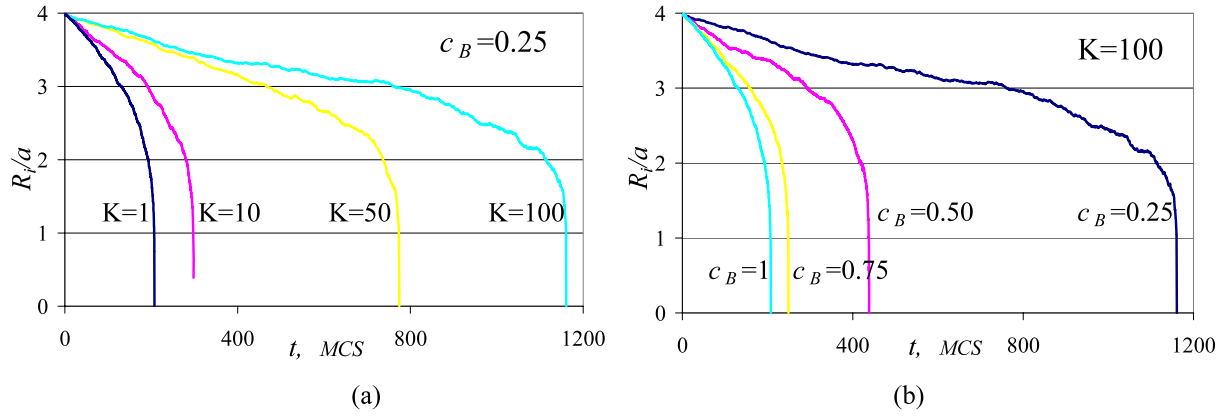

Figure 10. Collapse rate influenced by (a) ratio of frequencies and (b) volume fractions of components.

(Gibbs–Thomson effect) after formation of at least the first void inside. This void should appear due to the first driving force (a superposition of the chemical potential gradient and the difference of diffusivities).

(2) Conventionally, the critical void size is determined only by vacancy supersaturation and temperature. In our case, the concept of critical size should be reconsidered. Void behaviour, besides local vacancy concentration, is also determined by the gradients of vacancies and main component, so that a thermodynamically stable void might be kinetically unstable. An approximate criterion of central void growth is given by equation (25).

(3) In the process of inner void growth, the initial reserves of the chemical driving force (concentration and chemical potential gradients) run out, so that at some moment (at some void radius) the chemical driving force becomes less than the capillary forces (and the corresponding vacancy drop between the inner and external boundaries). Thus, one has a cross-over from formation to shrinking.

(4) In the general case, reaching the maximum void radius (end of formation and cross-over to shrinking) does not mean full homogenization, so that shrinking starts at once from an inhomogeneous shell. Therefore, separate treating of shrinking starting from a homogeneous initial hollow nanoshell is somewhat artificial and may lead to simulation artefacts, such as retardation, after some period of segregation. Of course, if the formation and shrinking proceed at different temperatures, some initial 'adjustment' of concentration profile at the beginning of shrinking might indeed have taken place.

(5) The formation stage starts from vacancy supersaturation just under the interface, and the formation of multiple tiny nanovoids in this region, with bridges in between providing mass-transfer to the remaining metallic core. (This feature was established only by Monte Carlo simulation, since our phenomenological model is spherically symmetric so far, and cannot describe the multiple voids and bridges.) This feature fully corresponds to the experimental data.

(6) The shrinking stage is characterized by the inverse Kirkendall effect: an outward vacancy flux generates the segregation of a faster component near the inner surface, the corresponding concentration gradient decreases the vacancy flux and, respectively, the shrinking rate. Thus, at the shrinking stage one also has the competition of capillary forces, assisting shrinking, and chemical forces, opposing shrinking. The peculiarity here is that the chemical force is not 'external', it is created by vacancy flux, generated by capillary forces. This result for a solid solution was obtained both by phenomenological

modelling and MC-simulation and coincides with results obtained by us earlier [8] for almost stoichiometric compounds with a narrow homogeneity range. The coincidence becomes almost perfect for the case of large absolute values of mixing enthalpy in a solid solution.

(7) For the case of large mixing enthalpies the steady-state approximation for the main components (not only for the vacancies) appears to be valid. For small and zero mixing enthalpies (an ideal solution) the steady-state approximation for the main components works worse.

(8) In this work we did not consider the reaction between solid nanoparticles and gases, the respective models will be presented elsewhere.

Acknowledgments

The work was supported by the Ministry of Education and Science of Ukraine, State Foundation of Fundamental Research (Ukraine), international bureau of BMBF (UKR 08/042) and the French-Ukrainian programme 'Dnipro'. Fruitful discussions with Professor K N Tu (UCLA) and Professor F Hodaj (INPG, Grenoble) are gratefully acknowledged.

References

[1] Aldinger F 1974 *Acta Metallogr.* **22** 923
[2] Geguzin Y E 1979 *Diffusion Zone* (Moscow: Nauka)
[3] Geguzin Y E, Klinchuk Yu I and Paritskaya L N 1977 *Fiz. Met. Metalloved.* **43** 602
[4] Yin Y, Rioux Robert M, Erdonmez Can K, Hughes S, Somorjai Gabor A and Alivisatos A P 2004 *Science* **30430** 711–4
[5] Yin Y, Erdonmez C K, Cabot A, Hughes S and Alivisatos A P 2006 *Adv. Funct. Mater.* **16** 1389–99
[6] Wang C M, Baer D R, Thomas L E, Amonette J E, Antony J, Qiang Y and Duscher G 2005 *J. Appl. Phys.* **98** 094308
[7] Tu K N and Gösele U 2005 *Appl. Phys. Lett.* **86** 093111
[8] Gusak A M, Zaporozhets T V, Tu K N and Gösele U 2005 *Phil. Mag.* **85** 4445–64
[9] Nakamura R, Tokozakura D, Lee J-G, Mori H and Nakajima H 2008 *Acta Mater.* **56** 5276–84
[10] Gusak A M and Tu K N 2009 *Acta Mater.* **57** 3367–73
[11] Nazarov A V and Gurov K P 1973 *Fiz. Met. Metalloved.* **37** 496
[12] Evteev A V, Levchenko E V, Belova I V and Murch G E 2008 *Def. Diffus. Forum* **277** 21
[13] Evteev A V, Levchenko E V, Belova I V and Murch G E 2007 *Phil. Mag.* **87** 3787
[14] Fan H J, Knez M, Scholz R, Hesse D, Nielsch K, Zacharias M and Gösele U 2007 *Nano Lett.* **7** 993–7